

# Magnetic Field Mapping of a Field Reversed Configuration Test Article

Ryan A. Pahl,<sup>1</sup> Warner C. Meeks,<sup>2</sup> and Joshua L. Rovey<sup>3</sup>  
*Missouri University of Science and Technology, Rolla, MO 65409*

Devices that form and accelerate field reversed configuration plasma may potentially be applied to spacecraft propulsion. Propulsion applications require heavy-gas plasma and the fundamental processes for heavy-gas field reversed configuration formation are still not well understood. Pre-ionization plasma properties are known to influence the success and final properties of field reversed configuration formation. In the following study the magnetic field of the pre-ionization stage of a heavy-gas field reversed configuration test article is presented. Initial results show discharge frequencies increase in the presence of plasma from 440 kHz in atmosphere discharges with no plasma to 472 kHz in 33 mTorr of air with plasma, both at an initial charge of 15 kV. Calibration of a three-axis magnetic field probe is completed using EMC Studio. Calibration values for the axial and azimuthal components of the probe are  $4.66 \times 10^8$  and  $9.45 \times 10^7$  G/V, respectfully. Magnetic field measurements at 15 and 20 kV are presented. The 15 and 20 kV discharges produce a peak current of 38 and 50 kA, respectfully. EMC simulations using these peak current values produce a maximum axial magnetic field of 632 and 819 G, respectfully. Measured axial magnetic field strengths of MPX at 15 and 20 kV using the B-dot probe yield 640 and 885 G, respectfully.

## Nomenclature

$A$	= Area, mm <sup>2</sup>
$B$	= Magnetic field, G
$B_{coil}$	= Magnetic field of theta coil, G
$\beta$	= Ratio of plasma particle pressure to external confining magnetic field pressure
$C$	= Capacitance, F
$\delta$	= Skin depth, m
$E_{cap}$	= Electrical energy stored in capacitor, J
$E_{ind}$	= Magnetic energy stored in inductor, J
$E_{input}$	= Energy input into plasma, J
$E_{ionization}$	= Energy required to ionize gas, J
$E_{loss}$	= Amount of energy due to loss mechanisms, J
$E_{thermal}$	= Thermal energy of plasma, J
$E_{thrust}$	= Amount of energy used to generate propulsive thrust, J
$I, i$	= Current, A
$L$	= Coil inductance, nH
$\mu$	= Magnetic permeability of conductor, H/m
$\mu_0$	= Magnetic permeability of free space, H/m
$n$	= Number of turns of wire
$\eta$	= Efficiency of energy conversion process to usable thrust
$R$	= Resistance, $\Omega$
$\rho$	= Resistivity of conductor, S/m

<sup>1</sup> Graduate Student, Mechanical and Aerospace Engineering, wcm994@mst.edu, Toomey Hall, 400 W. 13<sup>th</sup> St., Rolla, MO 65409-0050, and AIAA Student Member

<sup>2</sup> Graduate Student, Mechanical and Aerospace Engineering, rap4yd@mst.edu, Toomey Hall, 400 W. 13<sup>th</sup> St., Rolla, MO 65409-0050, and AIAA Student Member

<sup>3</sup> Assistant Professor, Mechanical and Aerospace Engineering, roveyj@mst.edu, Toomey Hall, 400 W. 13<sup>th</sup> St., Rolla, MO 65409-0050, and AIAA Senior Member

$t$	= time, s
$V$	= Voltage, V
$V_{probe}$	= Measured probe voltage, V
$\omega_0$	= Angular frequency, rad/s
$\omega_n$	= Natural angular frequency, rad/s

## I. Introduction

**F**IELD reversed configurations (FRCs) are a specific type of plasma configuration that is more generally known as a compact toroid. Compact toroids (CTs) include both spheromaks, which have toroidal and poloidal magnetic field ( $B_z \approx B_\theta$ ), and FRCs, which have only poloidal field ( $B_z \gg B_\theta$ ).<sup>1</sup> These plasma configurations are typically created using pulsed inductive circuits. Large currents ( $\sim kA$ ) are pulsed through strategically arranged inductive coils to induce a magnetic field and opposing plasma currents. The end goal of the creation process is magnetically self-contained plasma, meaning the plasma has internal currents creating a magnetic field detached from the applied field and the surrounding containment vessel. For propulsion applications, the magnetically detached CT (or plasmoid) is accelerated and expelled from the spacecraft generating thrust.

One of the benefits of a FRC device is that plasmoid acceleration (and thus thrust generation) is achieved via a JxB Lorentz force rather than an electrostatic potential. This means that FRCs are not space-charge limited, unlike gridded ion thrusters. Additionally, since FRCs use the mutual induction between the inductive coil and the plasma to deposit energy into the plasma and produce the JxB force needed to accelerate the plasmoid, no electrodes are needed. With minimal wall interaction and no electrodes, FRCs can avoid the technical challenges that plague other electric propulsion concepts.<sup>2</sup>

FRCs have potential for providing future spacecraft with a high thrust, high specific impulse ( $I_{sp}$ ) propulsion system. With their emergence in 1958,<sup>3</sup> FRCs started as an attractive fusion experiment due to their relatively high value of  $\beta$  ( $\approx 1$  at equilibrium),<sup>4</sup> where  $\beta$  is defined as the ratio of plasma particle pressure to external magnetic field pressure and these early systems were able to achieve plasmoid translation velocities of 170 km/s in deuterium.<sup>5</sup>

FRCs for space propulsion application have been previously investigated at the University of Washington, University of Alabama-Huntsville, and at the Air Force Research Laboratory (AFRL) at Edwards Air Force Base.<sup>6-13</sup> These studies have mainly focused on lower energy FRC formation and translation with higher atomic mass gases.

Research performed at the University of Washington has investigated the use of FRCs for space propulsion and fusion, both individually and as a combined spacecraft system. Slough, *et.al.*, have investigated the Propagating Magnetic Wave Plasma Accelerator (PMWAC) device for space propulsion<sup>6,7</sup> and also an earth-to-orbit fusion plasmoid device.<sup>8</sup> Both of these have similar operating principles. First, a FRC is created. Then the FRC is accelerated using a magnetic wave created by a sequence of pulsed electromagnetic coils. If the device is only providing propulsion, then the accelerated FRC is expelled at high velocity. However, if fusion is desired, then the FRC is compressed to smaller diameter causing the temperature to increase to fusion levels. Power can then be extracted for use creating the next FRC and the process is repeated. Results showed an ejection velocity of at least  $1.8 \times 10^5$  m/s for each deuterium plasmoid, which yielded a total impulse bit of 0.3 N-s.<sup>6</sup>

The University of Washington in collaboration with MSNW LLC is also developing the Electrodeless Lorentz Force (ELF) thruster. The goal of the ELF device is to demonstrate efficient acceleration of a variety of propellants to high velocities (10-40 km/s) and operation at high power (e.g.  $> 100$  kW). The device is designed around a conical geometry with a rotating magnetic field current drive to ionize the gas and drive an azimuthal current to form an FRC.<sup>14</sup>

Investigations at the University of Alabama-Huntsville and NASA Marshall Space Flight Center have centered on the Plasmoid Thruster Experiment (PTX).<sup>12,13,15,16</sup> PTX produces plasmoids in an analogous fashion to that shown in Fig. 2; however, a conical geometry is used instead of cylindrical. This geometry has benefits because the FRC creation and acceleration occur within the same step. Unlike the PMWAC developed by Slough, a traveling magnetic wave is not required to accelerate the FRC. Results have shown electron temperature and density of 7.6 eV, and  $5.0 \times 10^{13}$  cm<sup>-3</sup> for argon and 23 eV and  $1.2 \times 10^{14}$  cm<sup>-3</sup> for hydrogen.<sup>12</sup> Exit velocities up to  $2.0 \times 10^4$  m/s have been measured.

The electric propulsion group at Edwards Air Force Base constructed an annular FRC device called XOCOT.<sup>9</sup> The XOCOT project primary goal was to develop FRC-based plasmas at low power with long lifetime for propulsion applications. The program investigated different charging energies, voltages, and timing, as well as multiple propellants and pre-ionization techniques. Results showed multiple plasma formation and implosions are possible with densities and electron temperature on the order of  $3.0 \times 10^{13}$  cm<sup>-3</sup> and 8 eV, respectively.<sup>11</sup> Current Air Force efforts in collaboration with Michigan Technological University are focused on understanding and quantifying

the acceleration mechanism, plume profile, and plume energy of an FRC thruster.<sup>16</sup> XOCOT-T, the most recent version of the XOCOT experiment, is focused on the translation of FRCs formed at low voltages (0.5-3.0 kV) on longer time scales. This is accomplished with the use a three-turn conical outer coil and a pulsed gas puff valve. Several pressures and gas puff lengths have been investigated to determine optimal formation conditions.<sup>5</sup>

The Missouri Plasmoid Experiment (MPX) at Missouri University of Science & Technology is focused on the fundamental FRC formation physics in heavy-gases. Electric propulsion systems convert electrical energy into thrust. The efficiency of this conversion process can be written as Eqn. 1. In reality, input energy is converted to thrust, ionization (creating plasma species), thermal plasma energy (heating the plasma), and any loss processes, such as radiation and transport to walls. This is shown in Eqn. 2. To achieve high propulsion efficiency, the energy spent in the ionization, plasma heating, and loss processes must be small, however, ionization and plasma heating are necessary to produce the plasma propellant. The goal of an efficient electric propulsion system is to create as much plasma as possible using the least amount of energy, i.e., minimum ion production cost or maximum formation efficiency.

$$\eta = \frac{E_{thrust}}{E_{input}} \quad (1)$$

$$E_{input} = E_{thrust} + E_{ionization} + E_{thermal} + E_{loss} \quad (2)$$

The internal plasma mechanisms whereby input energy is converted to ionization, thermal energy, or lost from a heavy-gas FRC are poorly understood. As illustrated in Ens. 1 and 2, these processes are fundamentally important to achieving high propulsion efficiency.

The overall objective of the MPX is to elucidate the fundamental mechanisms that limit heavy-gas FRC formation efficiency. By studying the formation process, loss mechanisms, and energy profiles, models can be produced to better predict FRC formation and eventually lead to an optimized FRC configuration. In the present work, a high-frequency under-damped pulsed inductive theta pinch is used to breakdown and pre-ionize air. Presented studies are focused on thoroughly characterizing the pre-ionization plasma and magnetic field properties. Specifically, magnetic field maps of atmospheric discharging of the theta pinch circuit with and without plasma formation are measured and compared with numerical electrodynamic simulations. The following sections first describe the basics of FRC formation and the importance of pre-ionization plasma. Then the experimental setup is described. Next, results from internal magnetic field probes are compared to computer simulations using EMC Studio. Then a discussion and analysis of results is described. Finally the major conclusions are presented.

## II. Field Reversed Theta Pinch FRC Formation

The typical formation of a FRC using a field reversed theta pinch (FRTP) is a seemingly straight forward process and is illustrated in Fig. 1. Initially, the cylindrical containment vessel is filled with neutral gas and an initial bias field applied. Previous FRC experiments have used pressures ranging from 2-230 mTorr ( $0.065 - 7.46 \times 10^{15} \text{ cm}^{-3}$ );<sup>4,9,11,17,18</sup> however, it has been shown that a lower initial pressure tends to result in longer lasting FRCs with lower plasma temperatures being the trade off.<sup>17</sup> The bias field depicted in Stage II is generated by the theta coil and the diamagnetic current spools up in the weakly ionized plasma to counteract the applied field. The gas is ionized (pre-ionized), freezing the particles to the bias field lines. During Stage III the main capacitor bank is discharged, quickly reversing the applied magnetic field causing the magnetic field lines to

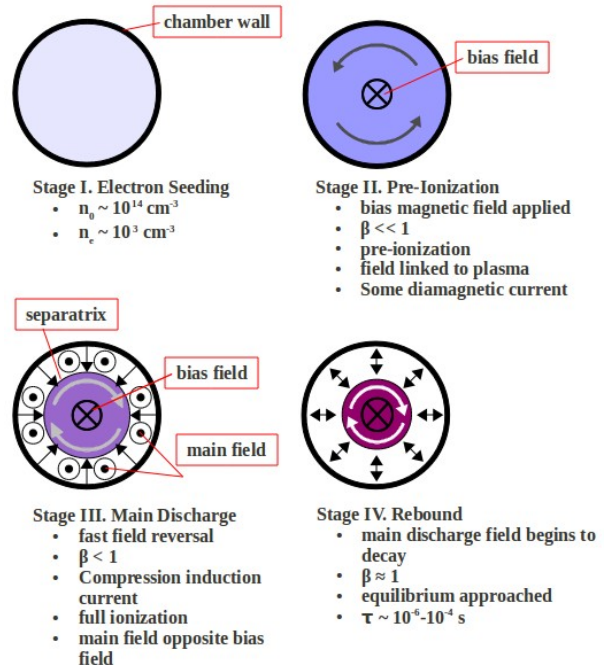


**Figure 1: FRC Formation Process using a Field Reversed Theta Pinch Coil**

“tear” and reconnect at the ends to form a self-contained plasmoid. The theta coil creates a magnetic field in the opposite direction as the bias field resulting in a strong  $J \times B$  force, compressing and heating the plasma. As the plasma compresses, the oppositely directed magnetic field lines reconnect near the ends of the coil forming the FRC. At this point, the FRC exists as a self-contained plasmoid and the separatrix (boundary that separates the distinct plasmoid from the area around it) can be clearly seen.

Next, the applied field compresses the plasmoid which begins to contract axially due to the strong concentration of magnetic fields lines at either end of the coil until the inward magnetic field pressure is balanced by the outward plasma particle pressure, reaching equilibrium as depicted in Stage IV. A schematic of an equilibrium FRC is shown in Figure 2.

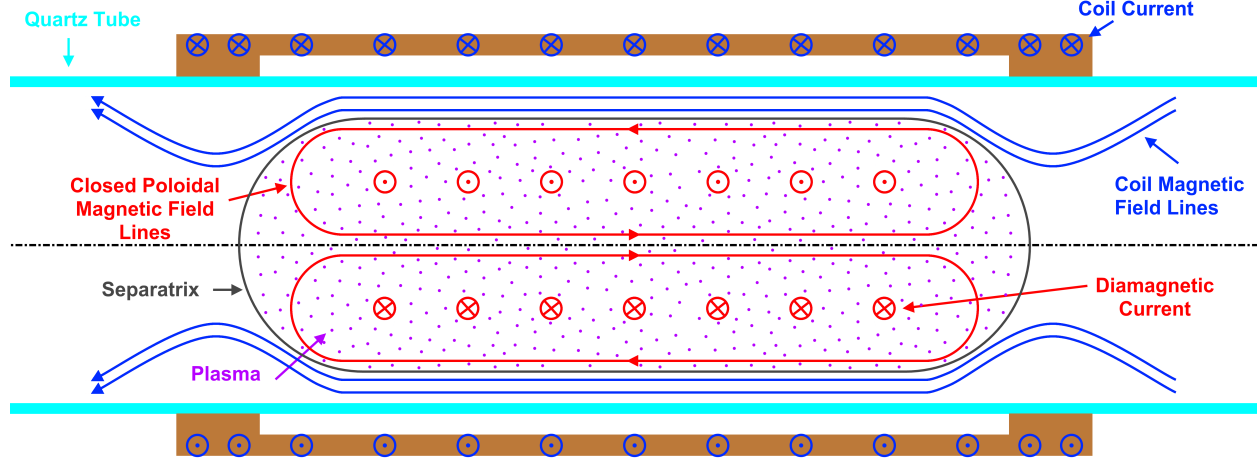


**Figure 2: A Field Reversed Configuration Plasmoid at Equilibrium**

Pre-ionization (Stage II in Figure 1) can be accomplished several ways. Tuszewski describes the introduction of axial and azimuthal currents, ringing quadrupoles, plasma injection, and laser irradiation, but goes on to state that while all of these methods have been shown to work, none of them show a clear superiority relative to the other methods.<sup>17</sup> While the pre-ionization of the plasma can be easily achieved, it has been shown that the FRC properties (stability, successful formation, end-state plasma properties) depend greatly on the specifics of the pre-ionization stage. This critical step is often overlooked, resulting in sporadic and inconsistent FRC formation.<sup>17</sup> The two most widely used techniques for pre-ionization are the axial and azimuthal pinch designs (Z-PI and θ-PI respectfully) due to their relative simplicity and occasionally employ seed ionization to reduce the energy requirement for the pre-ionization stage.<sup>17</sup>

It is the goal of MPX to use a field reversed theta pinch to form the FRC. The pre-ionization stage is the focus of the investigation presented in this paper. The MPX pre-ionization stage is a theta pinch that creates a strong time-varying magnetic field and associated electric field that breaks down (auto-ionizes) the gas. Seed electrons are not employed. Presented studies are focused on thoroughly characterizing the magnetic field properties of atmospheric discharges with and without plasma formation.

### III. Experimental Design and Setup

The study presented here uses the MPX FRC test article and multiple probes for measuring properties of the discharge circuit and magnetic field. First, the important design considerations used for the MPX are presented. Then details about the MPX test article are described. Next the pre-ionization theta pinch circuit is described. Finally, the probes used to acquire discharge circuit and magnetic field measurements are presented.

#### A. Design Considerations

Several criteria are considered when designing and constructing the MPX test article and pre-ionization circuitry: anticipated ion production cost, discharge circuit frequency, skin depth effects, stray inductance, and length-to-diameter ratio. The anticipated ion production cost is important for sizing the stored electrical energy and correspondingly the capacitance and voltage of the pre-ionization circuit. The initial system energy is contained entirely in the charged capacitor with total energy given by Eqn. 3. While the energy required to create one argon or xenon ion is theoretically 15.76 and 12.13 eV,<sup>19</sup> respectively, not all of the initial stored electrical energy is used for

ionized species production. During the discharge process, some of the initial stored electrical energy is lost to magnetic energy in stray parasitic inductance, resistive heating of circuit elements, and also plasma loss mechanisms, such as line radiation. The compounding effect of these loss mechanisms is to increase the energy required to create an argon or xenon ion. The energy required to create an ionized atom (ion production cost) is assumed to be 120 eV/ion based on previous experience with electric thruster and FRC plasma.<sup>10,20,21</sup> Using the anticipated ion production cost, the stored electrical energy is sized to be sufficient to ionize every atom within the test volume.

$$E_{cap} = \frac{1}{2} CV^2 \quad (3)$$

Discharge circuit frequency is also an important design criterion. In inductively coupled RF plasma, like the pulsed theta pinch investigated here, higher frequency is known to reduce the required magnetic field to break down and pre-ionize the gas. Figure 3 is a plot of breakdown magnetic field for different background pressure and device radii taken from the theoretical treatment of Burm.<sup>22</sup>

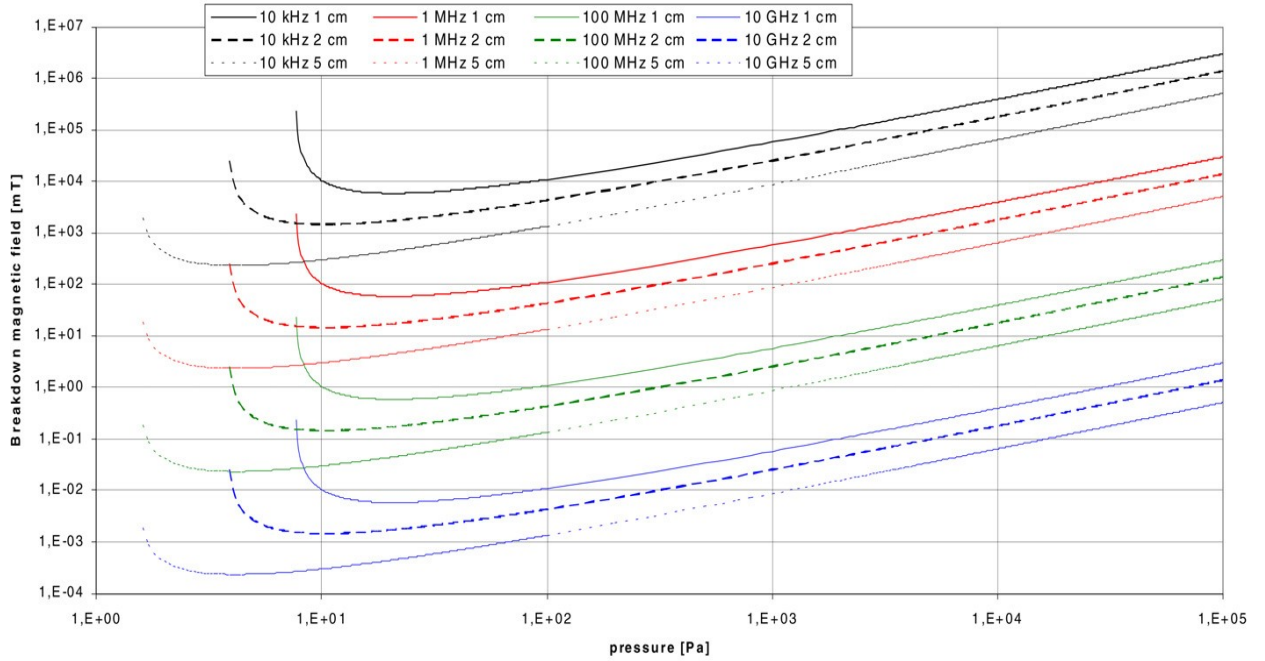


**Figure 3: Breakdown Magnetic Field Requirements for an Inductively Coupled Plasma<sup>22</sup>**

For example, a device with 1 cm radius requires a 10 T magnetic field to ionize argon at 10 kHz and 10 mTorr. Increasing the frequency to 1 MHz reduces the magnetic field requirement by two orders of magnitude to 0.1 T. Because the magnitude of the magnetic field is related to the magnitude of current flowing through the theta pinch, higher frequency also reduces the required magnitude of current. Assuming the discharge circuit is a series RLC circuit (detailed analysis presented in section V.A.), the frequency of the discharge circuit is given by Eqn. 4.

$$\omega_0 = \sqrt{\frac{1}{LC}} \quad (4)$$

Increasing frequency requires decreasing inductance and/or capacitance. A minimum level of inductance is set by the theta coil itself. The desire for low capacitance must be balanced with the stored energy requirements and anticipated ion production cost discussed above. Revisiting Eqn. 3 shows that to keep the same stored energy, as capacitance decreases voltage must increase. These considerations explain the need for high voltage in maintaining sufficient initial stored electrical energy while allowing capacitance to be low enough to achieve high frequency.

High frequency signals travel along the surface of conductors. This is known as the skin effect and the

penetration depth of the signal into the conductor is known as the skin depth. The skin depth is given by Eqn. 5<sup>23</sup>

$$\delta = \sqrt{\frac{2\rho}{\omega\mu}} , \quad (5)$$

where  $\rho$  is the resistivity of the conductor,  $\omega$  is the angular frequency, and  $\mu$  is the magnetic permeability of the conductor. To avoid enhanced resistance and associated resistive heating energy losses, the transmission line of a pulsed inductive circuit should have conductors that are at least as thick as a few skin depths. Further, fabricating conductors that are unnecessarily thick can also be avoided. Assuming a copper MPX theta coil with characteristic discharge frequency of 500 kHz, the skin depth is calculated to be 0.092 mm. To ensure rigidity of the transmission line and theta coil, copper with thickness of 1.5 mm is selected.

One of the goals of any FRC experiment is to deposit as much energy into the plasma as possible through the theta coil. Equation 6 relates the magnetic energy in an inductor and shows that it is directly proportional to its inductance.

$$E_{ina} = \frac{1}{2} LI^2 \quad (6)$$

To insure that the majority of the energy stored in the capacitor is deposited into the magnetic field of the coil, it is critical that the inductance of the coil is large when compared to the total circuit inductance. However, higher theta coil inductance drastically reduces the maximum discharge frequency (Eqn. 4), a critical component of RF discharge plasma formation. Therefore there is a trade-off between increasing the inductance so that a larger fraction of the stored electrical energy is converted to magnetic energy in the coil and the need for lower inductance to achieve high frequency to more easily pre-ionize the gas.

Formation chambers with larger length to diameter (L/D) ratios have been shown to produce more stable FRCs.<sup>17</sup> In general an L/D greater than three is desirable.<sup>17</sup> Having a larger L/D ratio better models the behavior of an ideal solenoid resulting in a more uniform magnetic field. Additionally, an increased L/D produces a larger mirror pinch at the coil end, confining the plasma within the theta coil.

**Table 1: MPX FRC Test Article Properties**

Property	Quartz Tube	Theta Coil
Material	214 Quartz	Copper
Number of Turns	N/A	1
Inner Diameter [mm (in)]	1545 (6.1)	178 (7.0)
Outer Diameter [mm (in)]	161 (6.3)	181 (7.1)
Thickness [mm (in)]	3.06 (0.12)	1.50 (0.06)
Length [mm (in)]	915 (36.0)	762 (30.0)
Inductance [nH]	N/A	37.2

## B. MPX FRC Test Article

The MPX FRC test article is a quartz tube surrounded by a cylindrical copper theta pinch shell. Properties of the tube and theta pinch shell are given in Table 1. A grade 214 quartz with an inner diameter of 154.5 mm, outer diameter of 160.7 mm, and a length of 915 mm is surrounded by a copper theta coil with inner diameter of 178 mm, length of 762 mm, and thickness of 1.5 mm. The coil is formed with 12.7 cm long tabs that span the length of the coil. These tabs allow for easier connection to the other circuit components. To ensure that the quartz tube is centered radially within the theta coil, 9.5 mm thick acrylic spacers are machined and inserted between the coil and the quartz at both ends of the test article. The quartz tube is connected to the vacuum facility in the Aerospace Plasma Lab at Missouri S&T. Relative to the quartz tube, the coil is mounted with a spacing of 8.3 cm from the vacuum chamber and 2.5 cm from the end cap

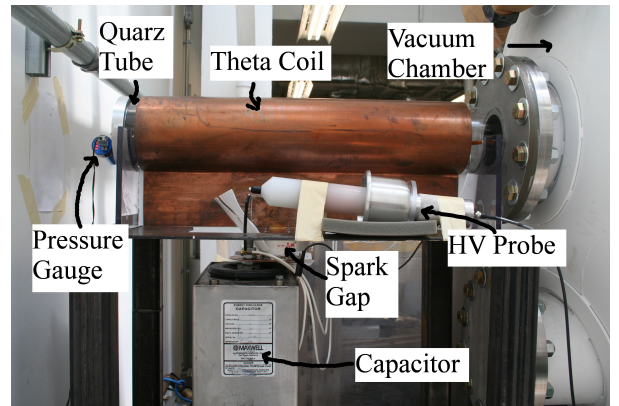


**Figure 4. MPX FRC test article attached to vacuum facility. Also shown are the high-voltage probe and pre-ionization capacitor.**

flange. The end cap is machined from aluminum and attaches to the quartz tube using a L-gasket. The theta coil has a L/D ratio of 4.29. A photograph of the test article is shown in Figure 4. A Lesker KJL275800 thermocouple gauge is used to measure internal pressure of the quartz tube and is mounted to the back of the end cap flange. A gas feed port is located at the center of the end cap flange to provide argon and xenon in future tests.

### C. Pre-Ionization Discharge Circuit

The pre-ionization capacitor bank is designed to fully ionize the gas within the volume of the quartz tube contained within the theta coil. Assuming an ion production cost of 120 eV/ion, to achieve 100% ionization of argon, a total energy of  $1.11 \times 10^{21}$  eV (178.1 J) must be deposited into the given volume of gas at a pressure of 20 mTorr. While ceramic capacitors offer the best high frequency characteristics and Q factors and therefore were the primary consideration for MPX, no off-the-self ceramic capacitors were found capable of providing these high energy levels. Investigations into connecting several ceramic capacitors in parallel were conducted, but the large number of capacitors required would have resulted in a very large stray inductance. Inquiries into a custom capacitor were conducted; however, the cost was prohibitive. As a result, an oil-filled capacitor is used for pre-ionization and its specifications are shown in Table 2. The maximum charging voltage of the pre-ionization stage of MPX is 25 kV, yielding a stored energy of 220.9 J. This is 124% of the energy needed to fully ionize the propellant assuming 120 eV/ion.

A simplified schematic of the pre-ionization circuit is shown in Fig. 5. The primary components of the pre-ionization circuit are the theta coil, capacitor, and spark gap switch. The capacitor is charged to an initial voltage level (15 and 20 kV in this paper) by a Matsusada RB30-30 power supply. A North Start PVM-5 (see D.1.) high voltage probe monitors the charge on the capacitor during both the charge and discharge stages. When the capacitor has reached the desired voltage, a Ross Engineering E40-2PNO high voltage switch is used to disconnect the power supply from the capacitor. An important note is that the connection is not only broken on the high voltage lead, but also on the ground lead. This isolates the capacitor from the charging system to prevent damage from high voltage and to ensure that the charging circuitry does not affect the discharge characteristics of MPX. After the charging system is disconnected, a PerkinElmer TR-1700 transformer steps-up a low voltage AC signal to 28 kV, triggering the GP-14B spark gap switch to close. The GP-14B is a high voltage, high current three-electrode switch produced by PerkinElmer. The trigger (T) and adjacent (A1, A2) electrodes are placed close together while the opposite (O) electrode is placed farther away. The positive side of the capacitor is connected to the adjacent electrode and the low voltage side to the opposite electrode. The high voltage signal from the transformer is applied between the trigger and adjacent electrodes, ionizing the gas within the device. The presence of the plasma allows the opposite and adjacent circuits to conduct, discharging the pre-ionization capacitor. A Pearson 4418 current monitor (see D.1.) is placed around the negative terminal of the capacitor and records the current waveform of the discharge.

### D. Probes and Data Acquisition

Two main types of probes are used in the study. Electrical circuit probes measure the discharge circuit voltage and current, while magnetic “B-dot” probes are used to record the pulsed magnetic field.

#### 1. Pre-Ionization Discharge Circuit Characteristics

The pre-ionization discharge circuit current and voltage characteristics are measured. Voltage is measured with a North Star PVM-5 high voltage probe with a 100-kV-pulsed maximum voltage, 80 MHz maximum frequency, and error at 500 kHz of less than 1.5%. The high voltage probe is connected to the high-voltage terminal of the capacitor, which is the high-voltage side of the spark-gap switch. Current is measured with a Pearson 4418 current

**Table 2: Pre-Ionization Capacitor Specifications**

Manufacturer	Maxwell
Voltage (kV)	70
Capacitance (uF)	0.707
Inductance (nH)	50

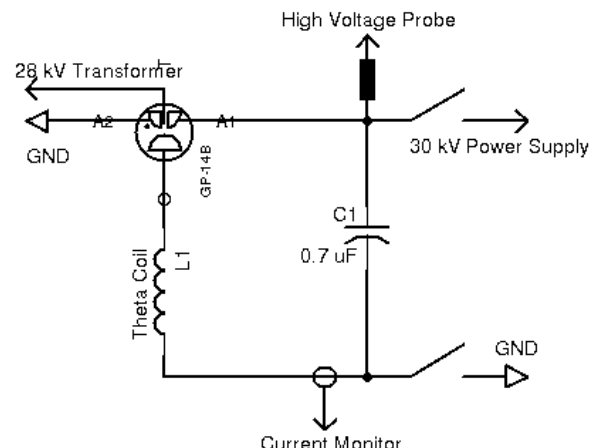


**Figure 5: MPX Pre-Ionization Circuit Diagram**

monitor with a peak current of 200 kA, maximum frequency of 2 MHz, and accuracy at 500 kHz of  $\pm 1\%$ . The current monitor is positioned around the negative terminal of the capacitor, which is connected to the capacitor body. A schematic showing the location of the probes is given in Figure 5. A summary of the probe specifications is provided in Table 3.

### 2. B-dot Probes

Magnetic probes are used to measure the magnetic field produced by the pulsed theta coil. A magnetic probe is basically a coil of wire. The physics of operation of magnetic probes (more commonly known as B-dot probes) is similar to a Rogowski coil and relies on Faraday's law. When the coil is placed within a time-varying magnetic field, a voltage is induced around the coil proportional to the number of turns,  $n$ , and cross-sectional area,  $A$ , through which the magnetic field is changing. This is expressed as Eqn. 7. Provided the "nA" constant for the probe is known, when the output of the probe is directly connected to an oscilloscope, the raw signal provides the time rate of change of the magnetic field. Integration of the raw signal then provides the magnetic field as a function of time,  $B(t)$ .

$$V_{probe} = n A \frac{dB_{coil}}{dt} \quad (7)$$

A three-axis magnetic probe is constructed and used to measure the magnetic field produced within MPX. The term "three-axis" is used to indicate that this probe actually consists of three coils, each oriented in a different spatial direction. Specifically, the three coils are oriented to record the magnetic field in the axial, radial, and azimuthal directions. Specifications of the probes are provided in Table 4. The final B-dot probe is shown in Fig. 6. Results and error analysis from calibration of this probe using a Helmholtz coil and numerical electrodynamics simulations is presented in subsequent sections.

The probe is mounted on a two-axis, R-Z motion control system inside the space simulation facility. Axial and radial translation stages are capable of traversing up to 100 and 40 cm, respectively. Both stages are driven with stepper motors controlled via LabView v8.6 through a National Instruments PCI-7334 motion controller connected to a National Instruments 4SX-411 nuDrive multi-axis power amplifier. With this setup the probe can be moved to different locations within the MPX internal volume, data collected, and a two dimensional map of the magnetic field obtained.

### 3. Data Acquisition

Data are acquired using a pair of 4-channel Tektronix DPO 2024 200 MHz 1 GS/s oscilloscopes that interface (via USB) with a dedicated 64-bit Windows 7 Enterprise workstation with Intel 3.0 GHz dual core CPU and 4 GB RAM. The same workstation is used to control the translation stages and probe location. After each pulse discharge, data are saved to the computer, then the probe location is adjusted with the translation stages and the next shot is prepared.

### E. Vacuum Facility

The vacuum facility is 6-ft-diameter, 10-ft-long and evacuated to rough vacuum by a Tokuda rotary vane pump connected to an Edwards blower. High-vacuum is achieved with four 35-inch-diameter Varian oil diffusion pumps with a combined pumping speed of 200,000 L/s on air. The MPX test article is attached to a 16-inch-diameter port on the rear of the facility. A custom flange has a machined groove and o-ring to seat and seal the quartz glass tube to

**Table 3: Electrical Properties of Current and Voltage Probes Used on MPX**

Manufacturer	North Star	Pearson
Model Number	PVM-5	4418
Max DC/AC Voltage (kV)	60 / 100	N/A
Max Current (kA)	N/A	200
Max Frequency (MHz)	80	2
Error at 500 kHz (%)	<1.5	$\pm 1$
Divider Ratio/Sensitivity	1000:1	1000:1

**Table 4: B-dot Probe Properties**

Axis	Area (mm <sup>2</sup> )	Turns	nA (mm <sup>2</sup> )
Axial (Z)	70.6	10	706
Radial (R)	46.8	20	936
Azimuthal ( $\theta$ )	29.8	20	595

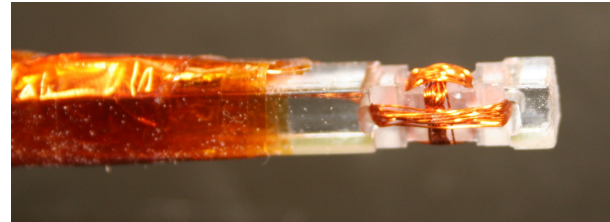


**Figure 6: B-Dot Probe**

the flange. A picture of the facility is shown in Figure 7.

#### IV. Results

The focus of the study presented here is the pre-ionization phase of RTP FRC formation and, specifically, to obtain magnetic field profiles within the MPX test article. Results from a Helmholtz coil analysis of the three-axis magnetic probe is presented. Then results from the MPX test article operated at atmospheric pressure conditions, and thus no plasma, are described. Both current and voltage waveforms are presented, as well as magnetic probe data. Finally, preliminary results from operation of the pre-ionization stage producing plasma are presented.

##### A. Helmholtz Coil Testing

Results from testing the three-axis B-dot probe at 10 kHz in a Helmholtz coil are presented. The following sections describe the coil, calibration, and results from B-dot probe testing.

###### 1. Helmholtz Coil

A Helmholtz coil is composed of two identical circular coils located on the same axis. The coils are placed a radius apart. When a current of the same magnitude and direction is supplied to both coils, a uniform magnetic field is created along the shared axis. Since a Helmholtz coil creates a uniform magnetic field, it is ideal for testing magnetic probes. The theoretical axial magnetic field is given by Eqn. 8, where  $\mu_0$  is the permeability of free space, I is the current in Amperes, and R is the radius in meters.

$$B = \left( \frac{4}{5} \right)^{\frac{3}{2}} \frac{\mu_0 n I}{R} \quad (8)$$

The Helmholtz coil used in these tests is a three inch diameter PVC tube with a wooden plug fit into the center. Fine wire (32 AWG) is tightly wound into two machined 10.1 mm<sup>2</sup> square cross section channels with an average radius of 42.9 mm yielding two very structured wire bundles (8 rows of 12 strands). Holes in the center of the Helmholtz coil, both axial and radially, allow for calibration of all three axes of the B-dot probe.

###### 2. Calibration

DC calibration of the Helmholtz coil (Fig. 8) is accomplished using an Allegro A1321 linear Hall effect sensor with a 5 mV/G sensitivity. The sensor is placed on the centerline of the Helmholtz coil. The current supplied to the coil is varied from zero to three amperes. The corresponding magnetic field is displayed in Fig. 8. The greatest error occurs at higher current levels. The



**Figure 7. Aerospace Plasma Laboratory Vacuum Chamber Facility**

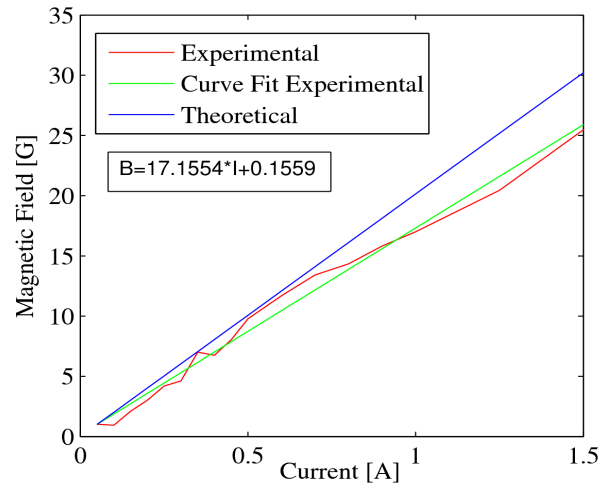


**Figure 8: Experimental Calibration of Helmholtz Coil**

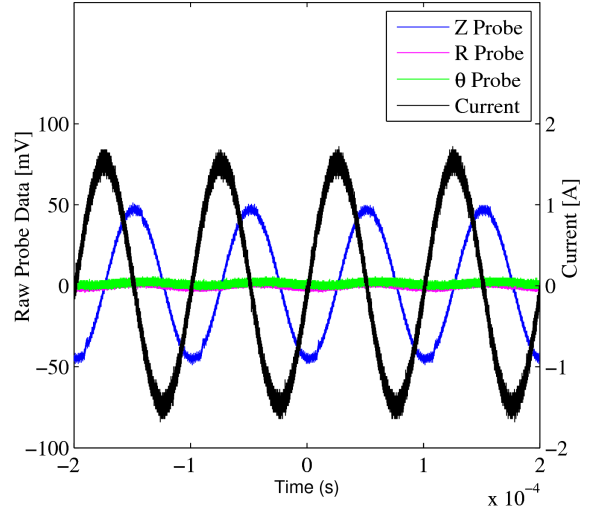


**Figure 9: B-dot Probe Calibration Data**

maximum error is 14%. For more information on DC calibration of a Helmholtz coil see Florian<sup>24</sup> and Smith.<sup>25</sup>

### 3. Results

Testing of the B-dot probes requires a time varying magnetic field. A function generator is connected to an amplifier and 1.52 amperes applied to the coil at 10 kHz. This current is supplying the two coils wired in parallel, so each 96-turn winding has a current of 0.76 A. From the DC calibration in Fig. 8, this current corresponds to 13.2 G. The three-axis B-dot probe is placed into this field and oriented so that only one probe is aligned with the magnetic field. Figure 9 shows the results when the axial B-dot probe is aligned with the field.

The axial (Z) probe shows the greatest response with a maximum of 51.5 mV. The radial (R) and azimuthal ( $\theta$ ) probes show maximums of 4.8 and 5.6 mV, respectfully. The low values of the radial and azimuthal directions illustrate that they are insensitive to changes in axial magnetic field. The high value of the axial component shows the probe is responsive to changes in the magnetic field in the direction it is designed for. Similar tests are conducted for the radial and azimuthal components using a radial through-hole in the center of the Helmholtz coil. By varying the orientation of the probe along this radial shaft, both the radial and azimuthal components of the magnetic field are found. The response of the azimuthal probe calibration is similar to that of the axial probe. Challenges in the calibration of the radial B-dot probe ultimately yielded no calibration value. Calibration factors for the B-dot probe at 10 kHz are presented in Table 5.

### B. Current-Voltage Characteristics

The MPX pre-ionization stage is discharged at atmospheric conditions with no plasma formation. Charging voltages of 15 kV and 20 kV are investigated. Current and voltage waveforms for 15 kV and 20 kV are presented in Figures 10 and 11, respectively. The voltage and current are under-damped waveforms exhibiting decaying oscillations. It is clear from both figures that the current lags the voltage by 90°, which is expected. For the 15 kV discharge, the peak current is 36.3 kA with a rise time of 0.57  $\mu$ s. The circuit completes approximately 16 full cycles before dampening out at approximately 37  $\mu$ s. For the 20 kV discharge, the peak current is 50 kA with a rise time of 0.57  $\mu$ s. The 20 kV test completes approximately 17 cycles before completely dampening to zero.

### C. Magnetic Field

The three-axis magnetic probe is used to obtain magnetic field measurements inside the MPX test article when the pre-ionization stage is discharged in atmospheric conditions without plasma formation and in low pressure conditions with plasma formation. Axial and azimuthal magnetic field values are recorded. Radial and axial probe motion is accomplished with the two-axis translation stage. Measurements are obtained in one cm increments in the axial direction and one cm increments in the radial direction. A location of  $(r,z) = (0,0)$  corresponds to the centerline and the end of the theta coil. Symmetry is assumed so only one quadrant of the coil is mapped. Therefore the maximum axial position is 38 cm. The maximum radial position is 4 cm. While the quartz tube has an inner radius of 7.7 cm, the

**Table 5: B-dot Calibration Factors at 10 kHz**

	Calibration Factor (G/V)
Axial (Z)	$8.6584 \times 10^6$
Azimuthal ( $\theta$ )	$1.6595 \times 10^8$

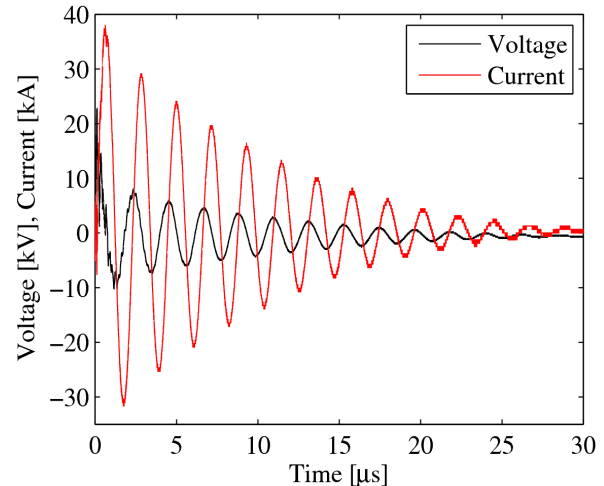


**Figure 10: MPX Atmospheric Discharge at 15 kV**

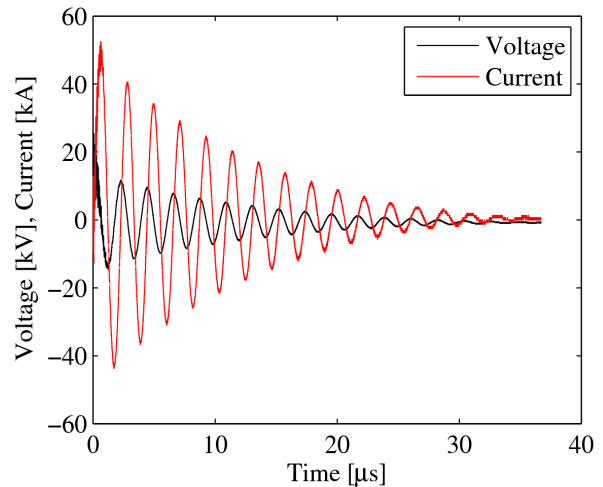


**Figure 11: MPX Atmospheric Discharge at 20 kV**

vacuum port and flange through which the probe protrudes has only a 6.5 cm radius. Future experiments may use an angled probe to capture data at larger radii.

Figure 12 shows the results of the magnetic mapping of MPX using the three-axis magnetic field probe. Measurements are normalized to the peak field strength. At the opening of the theta coil, the total axial field strength is approximately 60% of the maximum which occurs near the center of the coil. Figure 12 indicates that the field strength quickly increases along the axis of the coil for the first 25% of the length measured with the field strength leveling off near the center of the coil. The azimuthal direction is less than ten percent of the maximum field strength indicating that the theta coil is not perfectly cylindrical but may be approximated as such. The contour plot shown in Fig. 13 also confirms this trend. The magnetic field strength near the end of the coil is approximately 60% of the maximum field strength. The maximum field shown in Fig. 13 is also located at the center of the coil. Using the “quiver” function in MATLAB, component vectors indicating the combined axial and azimuthal direction of the magnetic field are shown. The axial component of magnetic field is clearly dominant; however, the azimuthal component of the magnetic field is clearly visible.

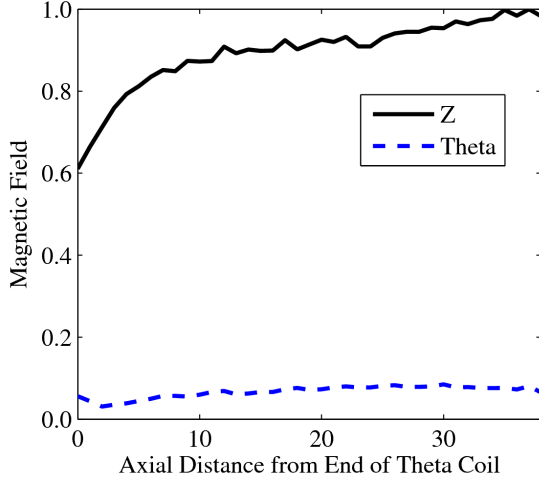


**Figure 12: Axial Magnetic Field Measurements in Atmosphere**

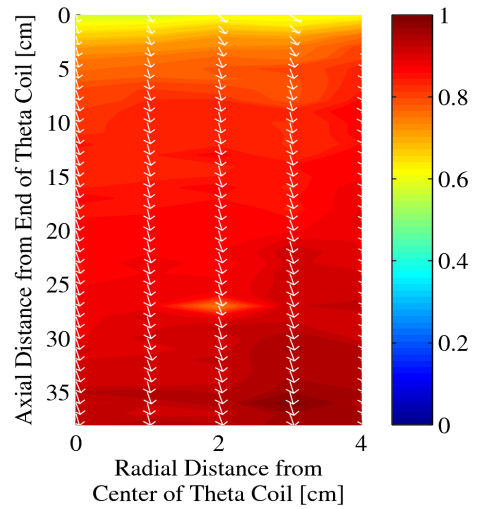


**Figure 13: MPX Magnetic Field Mapping at a Peak Current of 50 kA**

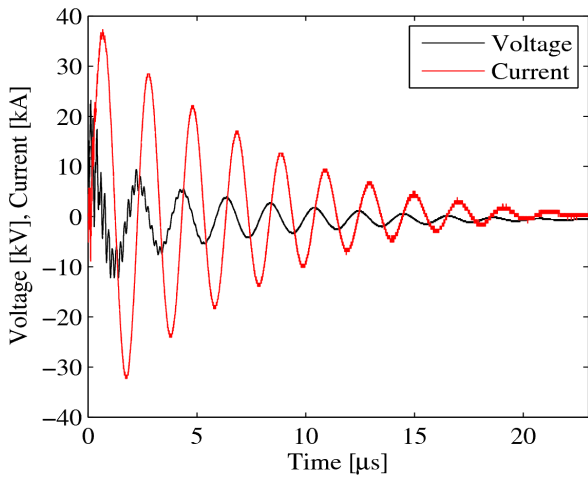


**Figure 14: Voltage and Current vs. Time of MPX Discharge at 15 kV in Air at 33 mTorr**

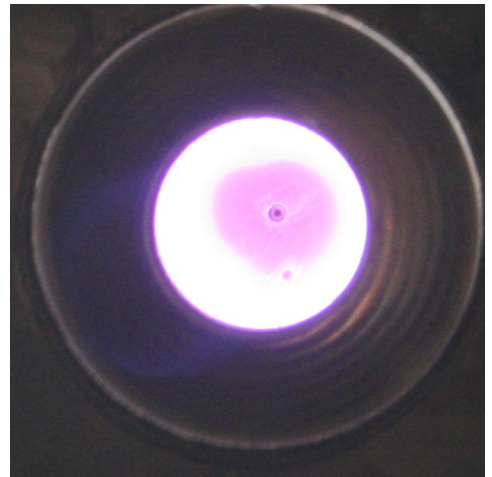


**Figure 15: MPX Plasma Discharge at 12 kV in 33 mTorr of Air**

#### D. Plasma Discharge

Preliminary plasma testing has yielded a few results to date. First, as shown in Fig. 14, the frequency of the MPX discharge in the presence of plasma is approximately 472 kHz, an increase of 7.2% over the atmospheric case. Additionally, plasma discharge still shots are captured using a Canon Rebel XT digital camera set for a long (seconds) exposure times to ensure that the discharge is captured. Figure 15 is a still shot with a two second exposure time. Due to the long exposure time, it is difficult to determine the formation process of the plasmoid; however, it appears that the plasma is formed along the wall of the coil and is concentrated near the walls. Without a side photo of the discharge it is impossible to know whether plasma formed along the entire length of the coil.

### V. Analysis and Discussion

Results from the MPX pre-ionization are compared to computer simulations conducted with both MATLAB and EMC Studio to shed light on the electrical properties of the pre-ionization circuit and to calibrate experimental magnetic field measurements, respectfully.

#### A. RLC Model Comparison

A simple series RLC circuit (Fig. 16) is used to model the theta pinch pulse. The governing equations are shown in Eqns. 9-12.<sup>26</sup>

Two discharges are presented to compare with the model: 15 kV discharges with and without plasma (Figs. 17 and 18, respectfully). Using the governing equations, a trial-and-error process yields circuit parameters that agree with the pre-ionization data to an accuracy of 1.7% on the amplitude of the first peak shown in Figures 17 and 18. The 15 kV discharge in atmosphere is modeled using an initial voltage of 20 kV, 50 mΩ resistance, and an inductance of 186 nH. To accurately model the pre-ionization stage during the 15 kV test with plasma, an

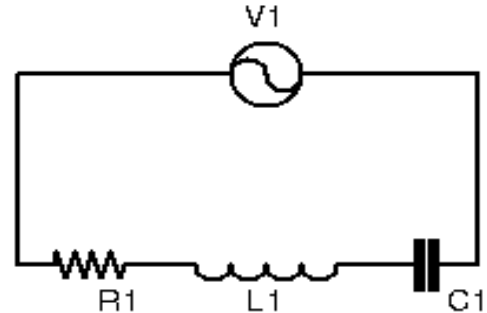


Figure 16: Series RLC Circuit

$$V_C(t) + V_R(t) + V_L(t) = 0 \quad (9)$$

$$L \frac{di(t)}{dt} + R \frac{di(t)}{dt} + \frac{1}{C} \int_0^t i(t) dt = 0 \quad (10)$$

$$\frac{d^2 i(t)}{dt^2} + \frac{R}{L} \frac{di(t)}{dt} + \frac{1}{LC} i(t) = 0 \quad (11)$$

$$\omega_n = \sqrt{\frac{1}{LC} - \left(\frac{R}{2L}\right)^2} \quad (12)$$

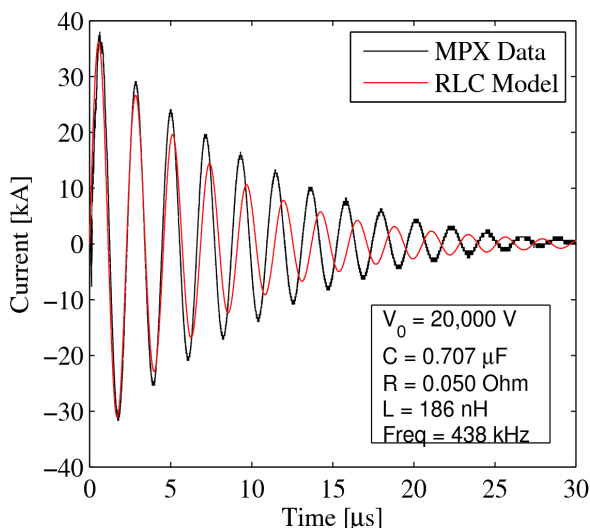


Figure 17: Comparison of RLC Model Current Predictions to Actual MPX Current Data at 15 kV in Atmosphere

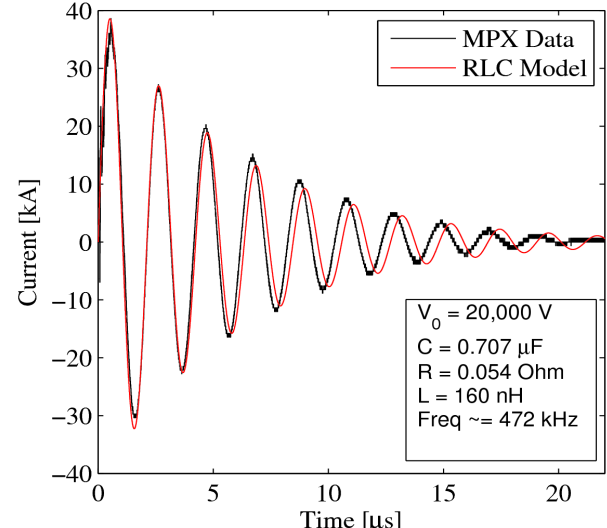


Figure 18: Comparison of RLC Model Current Predictions to Actual MPX Current Data at 15 kV with Plasma Present

initial voltage of 20 kV is used with a resistance of 54 mΩ, and an inductance of 160 nH. Both models used the same capacitance value of 0.707 μF. The discharge frequency of the pre-ionization stage of MPX at 15 kV in atmosphere with no plasma is approximately 440 kHz. The 15 kV discharge with plasma resulted in a discharge frequency of 472 kHz. This 7.3% increase in discharge frequency is attributed to the presence of plasma during this discharge.

To model both 15 kV discharges a 20 kV initial voltage is used. When using 15 kV as the initial condition, the peak current modeled is 28.5% below that of the MPX discharge. To match peak current values, a 20 kV initial voltage is necessary. This is believed to be due to a possible discrepancy in the voltage probe readings during the charge and discharge phases. When charging, the circuit is sharing a similar ground. After switching to discharge mode, however, MPX is designed to have a floating ground. The voltage probe is connected across the terminals of the capacitor and the signal fed directly into an oscilloscope. It is found that the grounding sheath of the coaxial cable connecting the scope to the probe is common to the low-voltage lead of the high voltage probe. It is possible that there is coupling from the probe and the scope that causes the probe to show one value on charge and a different value on discharge. This issue is currently being investigated and possible solutions are being considered.

An interesting thing to note from Figs. 17 and 18 is that while the model shows a constant frequency, it appears that the MPX discharge frequency starts slower than the model predicts during the first ring, matches on the second ring, and actually increases on later rings. To verify this, the model is used to determine the frequency of each peak on Fig. 18 and the results tabulated in Table 6. This analysis reveals that frequency of the discharge varies. The discharge frequency increases at a faster rate for the first few peaks and then begins to slow down. At the eighth peak the trend reverses and the frequency begins to decrease. This is believed to be independent of plasma formation because this change in discharge frequency is observed in with and without plasma present. However, this may be partially due to the effects of the spark gap. Energy is needed to energize the spark gap, allowing current to oscillate in the circuit. The majority of this energy is supplied from a triggering transformer over the course of 0.75 μs. It is possible that while the switch is opening (i.e., plasma is forming within the spark gap) the inductance of the spark gap is changing. Since the goal of MPX is to study the formation process, the model is made to agree best with the first two rings and later times neglected.

Finally, the inductance of the MPX pre-ionization stage and the predicted value from the model are analyzed. The model yields a total inductance of 186 and 160 nH for atmospheric and plasma tests, respectively. Comparing this with the calculated 37.17 nH inductance of the coil,<sup>3, 27</sup> it is apparent that at most 20% of the electrical energy stored in the capacitor is being deposited into magnetic energy in the coil during atmospheric tests. The listed capacitor and spark gap inductances are 50 nH and 5-30 nH, respectively. Returning to Eqn. 3, this means that roughly 106-131 nH of stray inductance is present. A significant contribution is likely due to the transmission lines that connect MPX to the capacitor.

## B. B-dot Probe Analysis

Analysis of the B-dot probes is done using the Helmholtz coil discussed previously and computer simulations in EMC Studio and compared with theory (Eqn. 8). An EMC Studio model is used to compare results from the experimental calibration. In the model, the Helmholtz coil is modeled in frequency domain using the EMC Studio suite to assist in B-dot probe analysis. To simplify modeling of the Helmholtz coil, cross sectional area of this channel is taken as the cross section of a larger, single turn coil. This yields a wire radius of 1.8 mm (roughly 7 AWG). Coil radius is made equal to that of the channel radial location of 44.5 mm and distance between coils is also replicated at the same 44.5 mm.

**Table 6: Changing Frequency of a Underdamped 15 kV Waveform in Plasma**

Peak Number	Inductance (nH)	Frequency (kHz)	Change in Frequency (kHz)
1	170.0	458.4	
2	160.0	472.4	14
3	155.0	480.0	7.6
4	153.0	483.1	3.1
5	152.0	484.7	1.6
6	151.0	486.3	1.6
7	151.0	486.3	0.0
8	151.5	485.5	-0.8
9	152.0	484.7	-0.8
10	152.5	483.9	-0.8

To define a current density equal to that of experiment it is noted that 96 (8x12 as mentioned above) total windings make up each of the two coils and that each winding is driven at 0.76 A. Therefore, assuming negligible space between wires, a single representative coil of equal total cross sectional area is driven at  $96 \times 0.76$  A, or 72.96 A to provide an approximately equal current density. Also equal to experiment, the coil simulation is driven at a frequency of 10 kHz. A probe array located at the zero radial location and spanning every 1 mm axially is used to report magnetic field values along the center of the Helmholtz coil. Figure 19 displays resultant magnetic field as a function of axial location for the center ( $r=0$ ) of the device. This figure demonstrates the reasonable degree of field magnitude consistency between the coils which are labeled at -22.2 and +22.2 mm axially. Field magnitude peaks at 15 G and remains nearly constant for a 20 mm distance (-10 to +10 mm) between the coils. Then a decrease in field magnitude can be seen near each coil until magnitude drops by 5% to 14.25 G at the coil axial locations. Theory gives a magnetic field of 15.3 G for a 0.76 A current. The error associated with the model and the Helmholtz coil at the driving current is 6.9%.

Calibration of the B-dot probe at high frequencies presents a challenge for the Helmholtz coil. An amplifier capable of driving the Helmholtz coil at frequencies of 500 kHz or greater while providing nearly an ampere of current is unavailable. Instead, a second method of calibration is employed. After validating the model and confirming a proficiency with modeling the physical characteristics of MPX, a model of the theta coil is made and compared to experimental values to determine a calibration factor for the B-dot probes. The cylindrical portion of the coil geometry is modeled with a 178 mm diameter and a 762 mm length. A gap of 9.3 mm is incorporated spanning the length of the cylinder. Rectangular tabs, also spanning the cylinder length of 762 mm, are then fixed to each gap edge extending, in parallel, a distance of 127 mm away from the cylinder. The physical structure of the coil is modeled to be a thin sheet to reduce computational difficulty at the edges during calculations. The electrical material properties however, are modeled with a thickness of 2 mm, a conductivity of  $10^7$  S/m, a magnetic permeability equal to that of vacuum, and a zero magnetic loss factor. Figure 20 illustrates this geometry. To the base of these tabs a simple time dependent current source is used to drive current through the entire device.

A double exponential wave form is used allowing a pulsed current to be introduced then decay naturally. A typical result from this wave form type is shown in Figure 21. This approach is taken to reduce

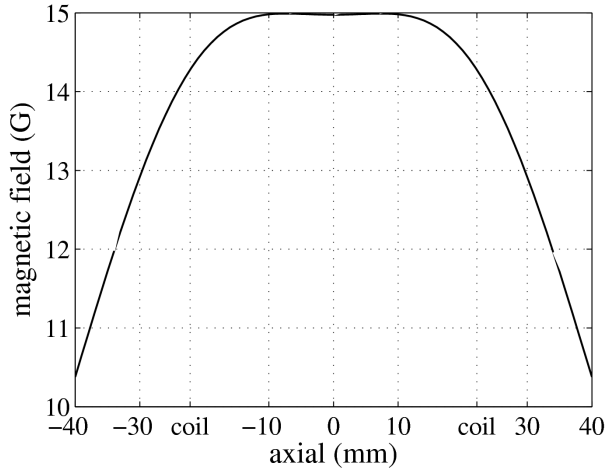


**Figure 19: Axial magnetic field profile**

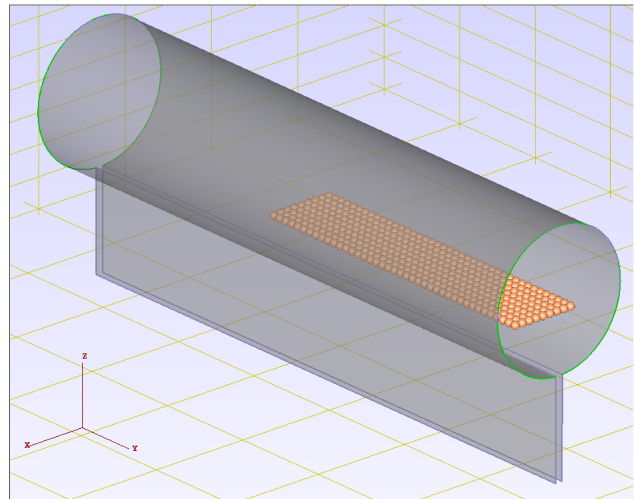


**Figure 20: isometric view of coil geometry taken from EMC Studio (includes field probe grid).**

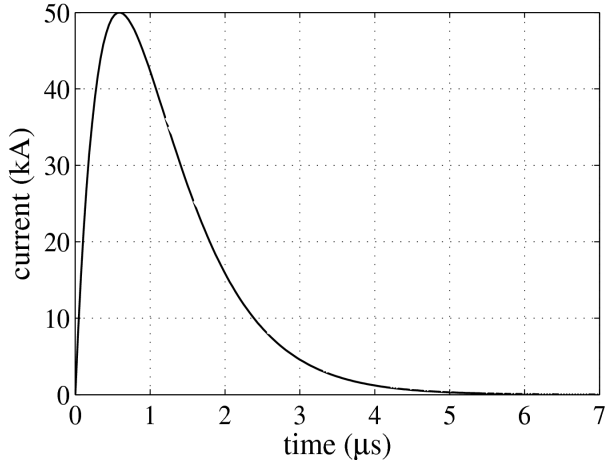


**Figure 21: Typical double exponential source pulse with peak of 50 kA at approximately 600 ns.**

computation time and is assumed to accurately describe the first quarter cycle of a sinusoidal ring with similar peak characteristics. Care is taken to model the pulse such that the time to reach peak current occurred at the same time as those found in MPX ringing data. Additionally, the amplitude is modeled to match that of MPX data as well. A field probe grid with a 1 cm spacing is employed from the center of the coil (both radially and axially) out to an axial distance of 400 mm and a radial distance of 80 mm. In reference to the coil then, the probe grid extends 19 mm past the coils axial edge and falls short of the coil radius by 8.9 mm. The probe grid can be seen along with the coil in Figure 20.

### C. Magnetic Field Comparison

The magnetic field of an ideal solenoid can be calculated using equation 13.

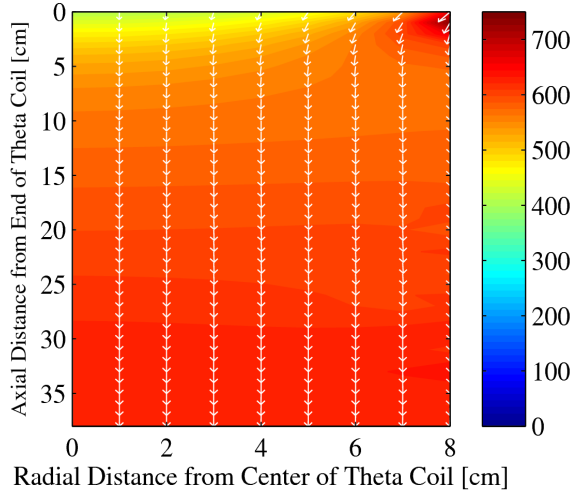


**Figure 22: EMC Studio Simulation of MPX Magnetic Field at a Peak Current of 38 kA**

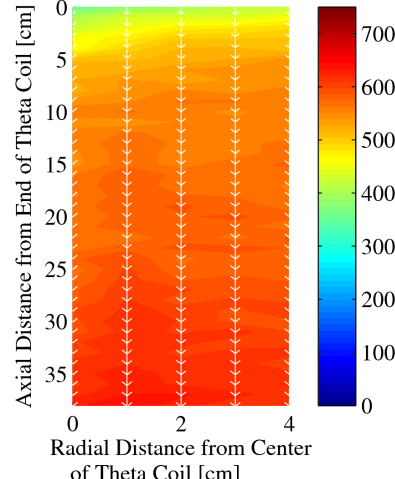


**Figure 23: MPX Magnetic Field Mapping at a Peak Current of 38 kA**

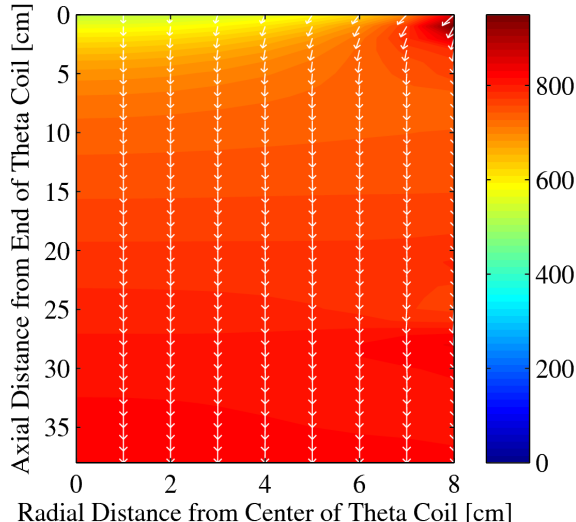


**Figure 24: EMC Studio Simulation of MPX Magnetic Field at a Peak Current of 50 kA**

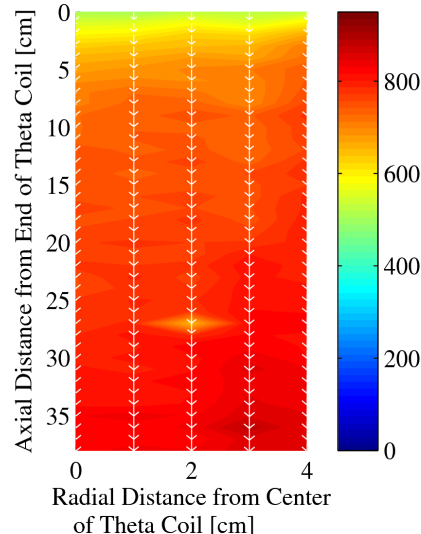


**Figure 25: MPX Magnetic Field Mapping at a Peak Current of 50 kA**

$$B = \frac{\mu_0 N I}{l} \quad (13)$$

Using the ideal solenoid equation, a maximum current of 50 kA produces a magnetic field of 874 G. Simulations using EMC Studio predict a max magnetic field of 819 G at the center of the coil along the centerline, a percent difference of 6.4%. The ideal solenoid equation assumes a solenoid of infinite length. Since the theta coil has a finite length, the field is expected to be smaller and have non-axial components of magnetic field at the ends of the coil due to end effects.

The magnetic field value at  $(r,z)=(0,38)$  in the center of the coil is compared to the integral of the B-dot data to give a calibration factor for the B-dot probe at 440 kHz. EMC Studio predicts a field of 819 G for a 50 kA peak discharge. The integrated signal from the axial B-dot probe yields a maximum of  $1.739 \times 10^{-6}$  V for a 38 kA peak discharge current. Taking the quotient of these values yields a calibration factor of  $4.7039 \times 10^8$  G/V for the axial probe. The calibration values of the remaining axes at 15 and 20 kV are shown in Table 7. The axial and azimuthal probes show the best agreement with only 2.2% maximum change in calibration factor between the 15 and 20 kV discharges. The radial probe shows inconsistencies far greater than either of the other probes and the calibration value is much smaller than either of the other probes. Testing the radial B-dot probe with the Helmholtz coil also yields similar results. No significant change is noticed when the radial probe is aligned with the field of the Helmholtz coil compared to its quiescent state. As a result, radial data will not be considered in these results.

The results of the simulation at both 15 and 20 kV are shown in Figures 22 and 24 and MPX data are shown in Figures 23 and 25. The 15 kV calibration values in Table 7 are used to calibrate the MPX data for both the 15 and 20 kV tests for comparison with the simulations. The 15 kV calibration value is used. The results of the simulation can be seen in Fig. 24. Fig. 25 is simply a resized version of Fig. 13 to properly match the scale of Fig. 24. Using a thin sheet assumption, it is clear that outside the theta coil the magnetic field is essentially zero and strongest in the center as expected. Furthermore, the direction of the magnetic field is axial inside of the theta coil. Near the end of the theta coil a slight bowing effect is seen which is due to the end effects of the solenoid which adds a slight radial component near the walls. While the end of the theta coil does see a pronounced decrease in field strength of approximately 40%, a region of increased field strength can be seen along the wall of the coil near the end. This increased field strength coupled with the addition of the radial component may be the beginning of a magnetic mirror effect; however, insufficient data are available to confirm this.

By comparing these figures, it is clear that the model accurately predicts the physical trends of the pre-ionization discharge magnetic field with no plasma. Using the calibration values in Table 7, magnetic field properties of MPX can be determined at any location. Figures 22 and 23 show the magnetic field map of the pre-ionization stage of MPX at 15 kV. The peak value in the EMC model occurs on the wall of the coil near the end of the coil. This is likely due to current pooling along the ends of the coil slightly increasing the local current density which results in an increased magnetic field. However, this can not be confirmed without wall data from the pre-ionization discharge. The remaining portion of Fig. 22 shows that the second strongest region of magnetic field is located near the center of the coil axially of 632 G. The experimental results of the 15 kV test in Fig. 23 show nearly identical trends. A field strength of 350 G near the opening of the coil increasing to a maximum field strength of 640 G at the center of the coil. Figures 24 and 25 show similar trends. Figure 24 does show a maximum field strength near the opening of the coil of approximately 923 G, the remaining field at the opening of the coil is 632 G. The field strength at the center of the coil is shown to be 819 G. This trend is nearly identical for Fig. 25. At the opening of the coil a field strength is 640 G is recorded and increases axially to 885 G at the center of the coil. The maximum and minimum magnetic field of the simulations and MPX are given in Table 8.

**Table 7: B-dot Probe Calibration Values**

	Calibration Value at 15 kV (G/V)	Calibration Value at 20 kV (G/V)	Error (%)
Axial (Z)	$4.6584 \times 10^8$	$4.7037 \times 10^8$	0.96
Radial (R)	$-3.0682 \times 10^5$	$-5.0969 \times 10^6$	94
Azimuthal ( $\theta$ )	$9.4538 \times 10^7$	$9.2480 \times 10^7$	2.2

**Table 8: Minimum and Maximum Magnetic Field Strengths of MPX**

		15 kV	20 kV
EMC Predicted Magnetic Fields (G)	Min	332	417
	Max	632	819
MPX Measured Magnetic Fields (G)	Min	350	500
	Max	640	885

## VI. Conclusions

This paper presents the key design considerations of the Missouri Plasmoid Experiment field reversed configuration formation study. Tests are conducted with an initial charge voltage of 15 and 20 kV with a 0.707  $\mu$ F capacitor providing 79.5 and 141 J of stored energy and peak currents of 38 and 50 kA, respectfully. Inductance of the theta coil is determined to be 37.2 nH. MPX circuit modeling yields a resistance of 50 m $\Omega$  and an inductance of 186 nH with a discharge frequency of 440 kHz without plasma. Magnetic field mapping of MPX shows maximum axial fields of 640 and 885 G for 15 and 20 kV discharges without plasma, respectfully.

The MPX pre-ionization discharge auto-ionizes air at 33 mTorr at 15 kV. A peak current of 38 kA is still observed. Circuit modeling gives a resistance of 54 m $\Omega$ , an inductance of 160 nH, and a discharge frequency of 472 kHz. The presence of plasma alters the I-V characteristics of the discharge. The discharge frequency increases from 440 kHz in atmosphere with no plasma to 472 kHz in the presence of plasma. The inductance decreases corresponding to the increase in frequency with 186 nH in atmosphere with no plasma to 160 nH at 33 mTorr in the presence of plasma. Significant stray inductance is present resulting in substantial energy losses. Up to 80% of the stored electrical energy is lost in stray inductance in atmospheric tests without plasma and 77% in the presence of plasma.

EMC Studio simulations accurately model the oscillating magnetic fields of a Helmholtz coil and are used to calibrate the B-dot probes. Simulations of a Helmholtz coil at 10 kHz yield a 15 G axial magnetic field. This result matches the 15.3 G given by Helmholtz coil theory within two percent, confirming its ability to adequately model MPX. Further EMC simulations of MPX at 38 and 50 kA are used to calibrate the B-dot probes with only a 2.2% change in calibration values between 15 and 20 kV tests. Simulations in EMC give similar peak values of 632 G for the 15 kV discharge and 819 G for 20 kV. The error between the 15 and 20 kV cases is 1.3 and 8.1%, respectfully.

The MPX pre-ionization stage is ready for further plasma and energy field characterization. Future tests will use air, nitrogen, argon, and xenon at multiple pressures to determine the effect of fill pressure on the plasma formation process. Later tests will also vary capacitor charging voltage to determine the effect of increased energy deposition into the plasma.

## Acknowledgements

The authors of this paper would like to thank the Air Force Office of Scientific Research (grant FA9550-10-1-0204, grant monitor Dr. Mitat Birkan) for funding this research.

## References

- 1 Bellan P.M., *Spheromaks: A Practical Application of Magnetohydrodynamic Dynamos and Plasma Self-Organization*, Imperial College Press, London, 2000.
- 2 Brown D.L., Beal B.E. and Haas J.M., "Air Force Research Laboratory High Power Electric Propulsion Technology Development," (2009).
- 3 Martin A. and Eskridge R., "Electrical Coupling Efficiency of Inductive Plasma Accelerators," *Journal of Physics D: Applied Physics*, Vol. 38, Nov, 2005, pp. 4168-4179.
- 4 Ruden E.L., Sanchez P.G., Taccetti J.M., Tuszewski M., Waganaar W.J., et al., "A High Density Field Reversed Configuration Plasma for Magnetized Target Fusion," Nov, 2003.
- 5 Niemela C.S. and Kirtley D.E., "Initial Results on an Annular Field Reversed Configuration Plasma Translation Experiment," Edwards AFB, CA, 2008.
- 6 Slough J.T. and Votroubek G., "Magnetically Accelerated Plasmoid (MAP) Propulsion," *42nd AIAA Joint Propulsion Conference*, AIAA 2006-4654, Sacramento, CA, July 9-12, 2006.
- 7 Slough J.T., "Propagating Magnetic Wave Plasma Accelerator (PMWAC) for Deep Space Exploration," (1999).
- 8 Slough J.T., "Earth to Orbit based on a Reciprocating Plasma Liner Compression of Fusion Plasmoids," *43rd AIAA Joint Propulsion Conference & Exhibit*, AIAA-2007-5130, Cincinnati, OH, July 8 - 11, 2007.
- 9 Kirtley D.E., Brown B., Gallimore A. and Haas J., "Details on an AFRL Field Reversed Configuration Plasma Device," *29th International Electric Propulsion Conference*, IEPC-2005-171, Princeton, NJ, Oct. 31 - Nov. 4, 2005.
- 10 Kirtley D.E., "Study of the Synchronous Operation of an Annular Field Reversed Configuration Plasma Device," Doctoral Thesis, Department of Aerospace Engineering, University of Michigan, 2008.
- 11 Kirtley D.E., Gallimore A., Haas J. and Reilly M., "High Density Magnetized Toroid Formation and Translation within XOCOT: An Annular Field Reversed Configuration Plasma Concept," *30th International Electric Propulsion Conference*, IEPC-2007-041, Florence, Italy, Sept. 17-20, 2007.

- 12 Koelfgen S.J., Eskridge R., Lee M.H., Martin A., Hawk C.C., et al., "Magnetic and Langmuir Probe Measurements on the Plasmoid Thruster Experiment (PTX)," *40th Joint Propulsion Conference*, AIAA-2004-4094, Fort Lauderdale, FL, July 11-14, 2004.
- 13 Koelfgen S.J., Hawk C.W., Eskridge R., Lee M.H., Martin A., et al., "A Plasmoid Thruster for Space Propulsion," *39th AIAA Joint Propulsion Conference*, AIAA 2003-4992, Huntsville, AL, July 20-23, 2003.
- 14 Slough J.T., Kirtley D. and Weber T., "Pulsed Plasmoid Propulsion: The ELF Thruster," *31th International Electric Propulsion Conference*, IEPC-2009-265, Ann Arbor, MI, Sept. 20-24, 2009.
- 15 Fimognari P.J., Cassibry J.T. and Ims K., "Effects of Pre-ionization and Bias Field on Plasmoid Formation and Acceleration," *43rd AIAA Joint Propulsion Conference*, AIAA 2007-5262, Cincinnati, OH, July 8-11, 2007.
- 16 Niemela C.S. and King L.B., "Numerical Optimization of an Annular Field Reversed Configuration Translation Experiment," *31st International Electric Propulsion Conference*, IEPC-2009-008, Ann Arbor, MI, Sept. 20-24, 2009.
- 17 Tuszewski M., "Field Reversed Configurations," *Nuclear Fusion*, Vol. 28, No. 11, 1988, pp. 2033-2092.
- 18 Rej D.J. and Tuszewski M., "A Zero-Dimensional Transport Model for Field-Reversed Configurations," *American Institute of Physics: Physics Fluids*, Vol. 27, June, 1984, pp. 1514-1520.
- 19 CRC Handbook of Chemistry and Physics. *90th edition*, 2009-2010.
- 20 Foster J.E. and Patterson M.J., "Enhanced Discharge Performance in a Ring Cusp Plasma Source," *26th International Electric Propulsion Conference*, IEPC-99-159, Kitakyushu, Japan, October 17-21, 1999.
- 21 Patterson M.J., "Performance Characteristics of Ring-Cusp Thrusters with Xenon Propellant," *22nd Joint Propulsion Conference*, AIAA-86-1392, Huntsville, AL, June 16-18, 1986.
- 22 Burm K., "Breakdown Magnetic Field in an Inductively Coupled Plasma," *Physics Letters A*, (2008), **372**: pp. 6280-6283.
- 23 Griffiths D.J., *Introduction to Electrodynamics*, Prentice-Hall, Inc., New Jersey, 1999.
- 24 Lucien F., "Bdot Plasma Probe," (2008).
- 25 Smith H.G., *Construction and Calibration of a Tri-Directional Magnetic Probe for the VASIMR Experiment on mini-RFTF*.
- 26 Hambley A.R., *Electrical Engineering: Principles and Applications*, Pearson Prentice Hall, 2008.
- 27 Lundin R., "A Handbook Formula for the Inductance of a Single-Layer Circular Coil," *Proceedings of the IEEE*, Vol. 73, No. 9, Sept., 1985, pp. 1428-1429.